Single-crystal elasticity of phase Egg $AlSiO_3OH$ and δ-AlOOH by Brillouin spectroscopy

Baoyun Wang[1,2,3,4], Yanyao Zhang[3], Suyu Fu[3], Li Li[1,4], Wen Liang[5], Maoshuang Song[1,4*] and Jung-Fu Lin[3*]

[1]State Key Laboratory of Isotope Geochemistry, Guangzhou Institute of Geochemistry, Chinese Academy of Sciences, Guangzhou 510640, China;

[2]College of Earth and Planetary Sciences, University of Chinese Academy of Sciences, Beijing, 100049, China;

[3]Department of Geological Sciences, Jackson School of Geosciences, The University of Texas at Austin, Austin, 78705 Texas, USA;

[4]CAS Center for Excellence in Deep Earth Science, Guangzhou, 510640, China

[5]Key Laboratory of High Temperature and High Pressure Study of the Earth's Interior, Institute of Geochemistry, Chinese Academy of Sciences, Guiyang 550081, China.

*Corresponding email: msong@gig.ac.cn and afu@jsg.utexas.edu

Abstract

The full elastic constants of phase Egg and δ-AlOOH have been determined by Brillouin scattering measurements at ambient condition. We find the phase Egg exhibits extremely anisotropic properties with azimuthal compressional wave anisotropy, AV_P =38.4% and shear wave splitting anisotropy, AV_S =22.1%, respectively, these values are higher than typical mantle minerals. Meanwhile, the anisotropy of δ-AlOOH is close to wadsleyite, but its aggregate velocity is faster than the majority of mantle minerals with the exception of stishovite and brigmanite, thus δ-AlOOH is a potential candidate for local positive abnormal seismic velocity in transition zone. In addition, the decomposition of phase Egg to δ-AlOOH and stishovite will lead to large velocity jumps of 17% for V_P and 18% for V_S based on present experimental elastic data at ambient condition, which is likely detectable by seismic observation in deep mantle of the earth.

Keywords: Phase Egg, δ-AlOOH, elasticity, anisotropy, Brillouin spectroscopy

Introduction

Hydrous phases (minerals) formed in wet subducted lithospheric slabs are regarded as potential carriers to transport water into deep earth interior. Dehydration of these hydrous phases can release substantial amount of water and significantly affect the physical and chemical properties of the surrounding rocks, such as partial melting, rheology and conductivity (Jacobsen, 2006; Ohtani, 2020). Based on advanced high-pressure and high-temperature apparatuses, researchers have examined phase relations on hydrous systems with various chemical compositions representing sedimentary, basaltic and peridotitic layers (components) of subducted slabs and a number of hydrous minerals have been identified (Iwamori, 2004; Litasov and Ohtani, 2003; Schmidt and Poli, 1998). Among these hydrous minerals, phase Egg and δ-AlOOH are two typical phases which exist in the sedimentary layer of subducted slabs or the simplified Al_2O_3+H_2O+SiO_2 ternary system (Ono, 1998; Schmidt et al., 1998). Besides, δ-AlOOH may even exist in basaltic and peridotitic layers (Suzuki et al., 2000). Experimental studies on the phase stability of phase Egg show it remains stable at depths of mantle transition zone (MTZ) along warm slab geotherm and then decomposes to δ-AlOOH and stishovite at depth of the upmost lower mantle (25-30GPa) (Fukuyama et al., 2017; Pamato et al., 2015; Sano et al., 2004). The δ-AlOOH is found to survive in the lower mantle down to core-mantle boundary conditions and even be stable along normal mantle geotherm (Duan et al., 2018; Ohtani et al., 2001; Sano et al., 2008; Yuan et al., 2019). Therefore, phase Egg and δ-AlOOH could form a continuous chain to transport water from MTZ to deep lower mantle in the process of slab subduction. The natural nano-size inclusions of phase Egg, which was discovered in ultradeep diamond (Wirth et al., 2007), provided the direct evidence for the existence of phase Egg at depth of mantle transition zone.

Phase Egg with an ideal formula of $AlSiO_3OH$ was firstly synthesized by (Eggleton et al., 1978). It belongs to monoclinic system with space group $\boldsymbol{P}2_1/n$

(Schmidt et al., 1998) and composed of layer arranged Si-octahedron and Al-octahedron (Figures S1a and b). High-pressure X-ray diffraction studies show that the compressibility of phase Egg is extremely anisotropic in three axis directions (Schulze et al., 2018; Vanpeteghem et al., 2003), which is also supported by recent *first-principles* calculation (Mookherjee et al., 2019). The δ-AlOOH is a synthetic high-pressure polymorphism of diaspore (α-AlOOH) and boehmite (γ-AlOOH), which adopts $CaCl_2$-type structure with $\boldsymbol{P}2_1nm$ space group (Figure S1c) (Suzuki et al., 2000). In recent years, increasing attention has been to δ-AlOOH due to its wide P-T stability field, pressure-induced hydrogen-bond symmetrization and formation of δ-phase AlOOH–FeOOH–$MgSiO_2(OH)_2$ –SiO_2 solid solution, which is of potential important significance to water circulation and dynamic evolution in the Earth's deep interior (Hsieh et al., 2020; Sano-Furukawa et al., 2018; Sano-Furukawa et al., 2009; Yuan et al., 2019). Elasticity data of phase Egg and δ-AlOOH is essential to interpret seismic (geophysical) observations and probe their possible existence and implication in the Earth's deep interior. Although first-principle calculation have been performed to calculate the elastic property of these two phases, few experimental study on their elasticity has ever been reported even at ambient condition. To date, only one Brillouin scattering study was performed on δ-AlOOH poly-crystalline aggregates (Mashino et al., 2016). Meanwhile, no experimental elastic data have be published for the phase Egg with the exception of buck moduli obtain from static compression X-ray diffraction (Schulze et al., 2018; Vanpeteghem et al., 2003).

In this study, we performed Brillouin scattering measurements on single crystal phase Egg and δ-AlOOH at ambient conditions. The full elastic tensors were extracted from the acoustic velocity using the Christoffell's equation. We quantify the compressional and shear wave velocities as well as the elastic anisotropy of phase Egg and δ-AlOOH, which will refine our understanding of the seismic feature of these two phases.

Experimental methods

Synthesis and characterization of single crystals

High-quality single crystals of Phase Egg and δ-AlOOH were synthesized at high pressures and high temperatures using the Sakura 2500-ton multi-anvil apparatus at Guangzhou Institute of Geochemistry, Chinese Academy of Sciences. To synthesize single-crystal phase Egg, a grounded mixture of CaO, $Al(OH)_3$ and SiO_2 in 1:4:2 mole ratio was used as starting material and sealed in an welded gold capsule. The synthesis experiment was conducted at 17 GPa and 1400 °C with a duration of 20 hours (run number U801). This experiment was initially intended to synthesize $CaAl_4Si_2O_{11}$, a Ca-rich aluminosilicate (Irifune et al., 1994; Zhai and Ito, 2008), but the recovered product turned out to be composed of single crystals of phase Egg with maximum dimensions of 200 μm and some fine powders. The chemical compositions of several crystals determined by electron microprobe analysis (EMPA) are 50.5(1) wt% SiO_2 and 41.7(1) wt% Al_2O_3, yielding a chemical formula of $Al_{0.98(1)}Si_{1.01(1)}O_4H_{1.02(1)}$ with the H content determined from the weight deficiency in total, which is close to the ideal formula of phase Egg. Single-crystal X-ray diffraction measurements also confirm that the synthesized crystals are phase Egg.

Single-crystal δ-AlOOH was synthesized by following the procedure reported by Kawazoe et al., 2017. Reagent-grade $Al(OH)_3$ powder of high purity (99.99%) was used as starting material and the synthesis experiment was conducted at 20 GPa and 1000 °C with a duration of 22 hours (run number U795). The recovered product is composed of crystals with a maximum dimension of about 300 μm. X-ray diffraction and EPMA measurments verified that the synthesized crystals are the pure phase of δ-AlOOH.

Sample preparation and Brillouin scattering measurements

To tightly constrain the elastic tensors of phase Egg (monoclinic, $\boldsymbol{P}2_1/n$) and δ-AlOOH (orthorhombic, $\boldsymbol{P}2_1nm$), which possess 13 and 9 elastic constants respectively, normally at least 3-4 platelets with different orientations are needed for Brillouin spectroscopic measurements on single-crystal elasticity. We carelfully checked the synthesized crystals under microscope and selected a number of high-quality clean and colourless crystals with homogeneous extinction for both phase Egg and δ-AlOOH. With the selected single crystals of phase Egg, we prepared four double-polished platelets with ~15um thickness. The Miller indexs of the polished faces of the four platelet, which were determined by traditional single crystal X-ray diffraction at the University of Texas at Austin, are (8, 3, -5), (0, -1, -1), (45, -6, 13) and (2, -1, 2). All four crystals displayed very similar lattice parameters and unit cell volumes, and the average values are: a = 7.1449(7), b = 4.3295(4), c = 6.9526(7), β = 98.35(9)°, and V_0 = 201.79(4) Å^3, which are consistent with the values reported by previous studies (Schulze et al., 2018; Vanpeteghem et al., 2003). The calculated density is 3.740(2) g/cm^3 with the measured unit-cell volume and the chemical formula mentioned above.

In case of δ-AlOOH, it was somehow difficult to prepare the platelets as the synthesized crystals are often twin crystals, preventing us to obtain a platelet of single crystal at some orientations. Fortunately, some twin crystals are large enough so as to allow us to collect Brillouin scattering signals from one single-crystal domain. Finally, we obtained three workable platelets with the Miller indexes (0, 0, 1), (2, 9, 2) and (10, 7, 3). The orientations of these platelets were determined by single-crystal X-ray diffraction measurements with a beam size of 3 × 4µm, which were performed at 13-IDD beamline sector of GSECARS at APS. The average lattice parameters of these three platelets are: a = 4.7093 (8), b = 4.2271 (1), c = 2.8302 (1) and V_0 = 56.34(5) Å^3, and the calculated density is 3.536(1) g/cm^3 with the measured lattice parameters and the chemical formula AlOOH.

Brillouin scattering measurements were conducted at ambient conditions using a Brillouin system at the Mineral Physics Laboratory, the University of Texas at Austin (Fu et al., 2017; Fu et al., 2019; Zhang et al., 2021). In the Brillouin system, a single-frequency 532 nm solid-state green laser (Coherent Verdi V2) was used as a excitation light source and a JRS six-pass tandem Fabry–Pérot interferometer equipped with a Perkin–Elmer photomultiplier detector was used to record the Brillouin spectra of the sample. Samples (platelets) were loaded in a short-symmetrical diamond-anvil cell without pressure transmitting medium. The laser beam was focused down to the sample in a spot approximately 20 μm in diameter. In a symmetric forward scattering geometry, sound (acoustic) velocities (v) were calculated from the measured Brillouin shifts (Δv) through the equation (Whitfield et al., 1976):

$$\mathrm{v} = \frac{\Delta\nu \cdot \lambda_0}{2\sin(\theta/2)}$$

where v is the acoustic velocity, $\Delta\nu$ is the measured Brillouin frequency shift, λ_0 is the laser wavelength of 532 nm, and θ is the external scattering angle of 48.3° .

Results and discussion

Phase Egg

Brillouin scattering measurements were performed for each platelet of phase Egg in 19 distinct directions at an interval of 10° over an angular range of 180°. One typical Brillouin spectrum is shown in Figure 1a. In most cases, both compressional acoustic mode (V_P) and shear acoustic modes (V_S1, V_S2) can be observed, but the V_P signal was blocked by the strong V_S peak of diamond at some directions. The dispersion of measured acoustic velocities with azimuthal angle for the four platelets of phase Egg are depicted in Figure 2. Using the density from the single-crystal X-ray diffraction measurements and the sound velocities as a function of azimuthal angle measured by Brillouin scattering, we inverted the 13 independent elastic constants of phase Egg by using a nonlinear least-squares fitting to the Chritoffel's equation (Every, 1980). In the procedure of inversion, we used the C_{ij} values calculated by *first-principals* simulation as the initial values (Mookherjee et al., 2019). All the elastic constants based on the Cartesian coordinated system where the *X*-axis parallel to *a**-axis and *Y*-axis parallel to *b*-axis are obtained after several fitting runs. The inverted results of elastic constants C_{ij} for phase Egg are given in Table 1, together with the theoretical values (Mookherjee et al., 2019). Our results are generally in agreement with those of Mookherjee et al., 2019, but all of our principal C_{ij} are much lower than the theoretical values.

The principal elastic constants exhibit a relation of $C_{11}>C_{33}>C_{22}$, while the shear elastic components holds a relation of $C_{55}>C_{66}>C_{44}$. These relations can be well explained by the orientation of the hydrogen bond, which is mostly aligned along the *b*-axis but is tilted to have a component along the c-axis of the crystal structure, and the distortion of SiO_6 octahedron with the longer Si-O(4) bond lying in the a-c plane (Schmidt et al., 1998; Schulze et al., 2018) (Fig. S1 a and b). The values of the principal elastic constants with C_{11} being twice as much as C_{22} indicate that phase Egg has a striking anisotropy in axial compressibility and *b*-axis is the most compressible direction, in agreement with the observations by previous static compression experiments (Schulze et al., 2018; Vanpeteghem et al., 2003).

The measured elastic constants of phase Egg allow us to evaluate its azimuthal anisotropy of acoustic velocity. From 3D azimuthal imaging of velocity distribution (Figure S2), it is noticed that the compressional-wave velocity varies from 7.68 km/s to 11.34 km/s. The fastest compressional-wave velocity propagates along the direction that deviates 38° to *a*-axi in *a-c* plane, and slowest compressional-wave velocity propagates along the *b*-axis direction. Similarly, the shear-wave velocity also exhibits strong dependence on directions (anisotropy). The anisotropy factors of compressional-wave and shear-wave velocities, $AV=200\times(V_{max}-V_{min})/(V_{max}+V_{min})$, are calculated to be AV_P = 38.4% , AV_{S1} = 21.3% and AV_{S2} = 21.2, and the shear-wave splitting factor, which is defined as $AV_S=200\times(V_{S1}-V_{S2})/(V_{S1}+V_{S2})$， is calculated to be 22.1%. Using the Voigt–Reuss–Hill averages, the aggregate properties such as adiabatic bulk and moduli as well as the aggregate compressional-wave and shear-wave velocities are also calculated and given in Table 1.

δ-AlOOH

Figure 1b show a representative Brillouin spectrum of δ-AlOOH. The measured acoustic velocities as a function of azimuthal angle for the three δ-AlOOH platelets are shown in Figure 3. The full 9 independent elastic constants of δ-AlOOH were inverted by fitting all the velocity data of the three platelets using the Christoffel's equation and the results are given in Table 1. Our values of the elastic constants are in good agreement with the theoretical values using *first- principals* simulations (Tsuchiya and Tsuchiya, 2009). We found the principal elastic constants hold the relation $C_{33}>C_{11}>C_{22}$ and C_{22} are much smaller than C_{33} and C_{11}. In accordance with this relation, the velocity along the *c*-axis is faster than *a*-axis and *b*-axis by about 7.4% and 21.1%, respectively. The relation of $C_{33}>C_{11}>C_{22}$ reflects the anisotropy in axial compressibility in the crystal structure of δ-AlOOH which is consistent the fact that the O-H bond lie in the *a-b* plane (see Figure S1c), hence a- and b-axes are more compressible than c-axis. The anisotropic factors of δ-AlOOH are calculated and yield values of AV_P = 19.1%, AV_{S1} = 6.89 and AV_{S1} = 6.56. The shear-wave splitting factor is calculated to be AV_S = 12.65%. The calculated isotropic aggregate properties of δ-AlOOH are shown Table 1. Interestingly, the aggregate V_P and V_S values in our study are higher by 5.2% and 8.8% respectively than those determined by Brillouin scattering measurements on polycrystalline aggregate of δ-AlOOH (Mashino et al., 2016). Previous study shown the size of the polycrystalline aggregate sample influence significantly the obtained velocity in Brillouin scattering measurements. For example, large reductions of compressional and shear wave velocities were observed in the nanocrystalline MgO (Gleason et al., 2011; Marquardt et al., 2011). In this sense, the discrepancy between our results and Mashino's et al. (2016) probably also originated from the size effect of polycrystalline δ-AlOOH, which deserved further study to clarify this issue in future.

Implications

Seismology is one of the primary methods for investigating water circulation in the earth's interior. To date, many elasticity studies have been carried out on the major water-bearing mantle minerals, such as olivine, wadsleyite and ringwoodite (Jacobsen et al., 2008; Mao et al., 2008b; Mao et al., 2012). Although the amounts of hydrous phase Egg and δ-AlOOH are not high with comparison to major mantle minerals, it is also possible to detect them by seismic observations if they exhibit remarkable contrast of seismic property to their surrounding rocks in subduction zone. We have compiled the density, aggregate elastic moduli, aggregate acoustic velocities and anisotropy factors of typical minerals in subducted slabs together with phase Egg and δ-AlOOH at ambient condition (Fan et al., 2020; Fan et al., 2019; Jackson et al., 2006; Jiang et al., 2009; Mao et al., 2015; Mao et al., 2008a; Mao et al., 2012; Sanchez-Valle et al., 2019; Sinogeikin et al., 1998; Sinogeikin et al., 2004; Wang et al., 2014; Wu et al., 2016; Zhang and Bass, 2016)(See Table S1). It is found that the density, elastic moduli and acoustic velocities of phase Egg are quite close to that of ferropericlase with 6wt% iron, but the phase Egg exhibits larger anisotropy of compressional-wave velocity (AV_P). Actually, the AV_P of phase Egg is higher than that of all the other minerals. Therefore, it is likely phase Egg is a potential candidate of seismic anisotropy of compressional-wave velocity in subducting slabs. As for δ-AlOOH, its V_P are faster than all the other major minerals in subducted slabs except stishovite and bidgmanite, and its V_S is close to bidgmanite. Thus δ-AlOOH may result in high-velocity anomaly at depths of mantle transition zone. As mentioned before, with pressure increasing, phase Egg will decompose to δ-AlOOH and stishovite at the depth of the uppermost lower mantle along slab geotherm through the reaction: $AlSi_3OH$=δ-AlOOH+SiO_2. Based on the elastic data obtained at ambient conditions in this study, the velocity contrast of this reaction are determined to be 17% for V_P and 18% for V_S, respectively, which is likely detectable by seismic observation in deep mantle of the earth.

It should to be stressed that above conclusions require to be further refined by elasticity experiments when being applied to seismic observations in the deep earth's interior. Pressure and temperature are two important thermal parameters which influence the elasticity of materials. In particular, recent *first-principals* calculations shows the evolution of elastic properties with pressure is abnormal due to the hardening behavior of hydrogen bond. In the case of δ-AlOOH, the pressure-induced symmetrization of hydrogen bond was observed and hardening effect of hydrogen-bond symmetrization on elastic constants was unveiled by Brillouin scattering study on polycrystalline aggregate and first-principals theoretical study (Mashino et al., 2016; Tsuchiya and Tsuchiya, 2009). Meanwhile, pressure-induced transfer of hydrogen between acceptor and donor was proposed by recent study (Mookherjee et al., 2019), which is interpreted to affect significantly the elastic constants of phase Egg at high pressure. Because the abnormal behaviors of hydrogen bond probably occurs in the earth's interior for phase Egg and δ-AlOOH, further in-situ high-pressure and high-temperature elasticity experiments are needed to explore the elastic behavior of these two hydrous minerals under extreme conditions of the earth's deep interior.

Acknowledgments

We would like to thank Vincent Lynch for measuring the crystal orientations of phase Egg. The single-crystal X-ray diffraction of δ-AlOOH were performed at 13-IDD beamline of GSECARS. M. Song acknowledges financial support from the Strategic Priority Research Program (B) of Chinese Academy of Sciences (Grant No. XDB18000000) and the National Natural Science Foundation of China (Grants No. 41874107, 41574079).

References

Duan, Y., Sun, N., Wang, S., Li, X., Guo, X., Ni, H., Prakapenka, V.B., and Mao, Z. (2018) Phase stability and thermal equation of state of δ-AlOOH: Implication for water transportation to the Deep Lower Mantle. Earth and Planetary Science Letters, 494, 92-98.

Eggleton, R.A., Boland, J.N., and Ringwood, A.E. (1978) HIGH-PRESSURE SYNTHESIS OF A NEW ALUMINUM SILICATE - AL5SI5O17(OH). Geochemical Journal, 12(3), 191-194.

Every, A. (1980) General closed-form expressions for acoustic waves in elastically anisotropic solids. Physical Review B, 22(4), 1746.

Fan, D., Fu, S., Lu, C., Xu, J., Zhang, Y., Tkachev, S.N., Prakapenka, V.B., and Lin, J.-F. (2020) Elasticity of single-crystal Fe-enriched diopside at high-pressure conditions: Implications for the origin of upper mantle low-velocity zones. American Mineralogist: Journal of Earth and Planetary Materials, 105(3), 363-374.

Fan, D., Xu, J., Lu, C., Tkachev, S.N., Li, B., Ye, Z., Huang, S., Prakapenka, V.B., and Zhou, W. (2019) Elasticity of single-crystal low water content hydrous pyrope at high-pressure and high-temperature conditions. American Mineralogist: Journal of Earth and Planetary Materials, 104(7), 1022-1031.

Fu, S., Yang, J., and Lin, J.-F. (2017) Abnormal elasticity of single-crystal magnesiosiderite across the spin transition in Earth's lower mantle. Physical review letters, 118(3), 036402.

Fu, S., Yang, J., Tsujino, N., Okuchi, T., Purevjav, N., and Lin, J.-F. (2019) Single-crystal elasticity of (Al, Fe)-bearing bridgmanite and seismic shear wave radial

anisotropy at the topmost lower mantle. Earth and Planetary Science Letters, 518, 116-126.
Fukuyama, K., Ohtani, E., Shibazaki, Y., Kagi, H., and Suzuki, A. (2017) Stability field of phase Egg, AlSiO3OH at high pressure and high temperature: possible water reservoir in mantle transition zone. Journal of Mineralogical and Petrological Sciences, 112(1), 31-35.
Gleason, A.E., Marquardt, H., Chen, B., Speziale, S., Wu, J., and Jeanloz, R. (2011) Anomalous sound velocities in polycrystalline MgO under non-hydrostatic compression. Geophysical Research Letters, 38.
Hsieh, W.P., Ishii, T., Chao, K.H., Tsuchiya, J., Deschamps, F., and Ohtani, E. (2020) Spin transition of iron in δ-(Al, Fe) OOH induces thermal anomalies in Earth's lower mantle. Geophysical Research Letters, 47(4), e2020GL087036.
Irifune, T., Ringwood, A.E., and Hibberson, W.O. (1994) SUBDUCTION OF CONTINENTAL-CRUST AND TERRIGENOUS AND PELAGIC SEDIMENTS - AN EXPERIMENTAL-STUDY. Earth and Planetary Science Letters, 126(4), 351-368.
Iwamori, H. (2004) Phase relations of peridotites under H2O-saturated conditions and ability of subducting plates for transportation of H2O. Earth and Planetary Science Letters, 227(1-2), 57-71.
Jackson, J.M., Sinogeikin, S.V., Jacobsen, S.D., Reichmann, H.J., Mackwell, S.J., and Bass, J.D. (2006) Single-crystal elasticity and sound velocities of (Mg0. 94Fe0. 06) O ferropericlase to 20 GPa. Journal of Geophysical Research: Solid Earth, 111(B9).
Jacobsen, S.D. (2006) Effect of water on the equation of state of nominally anhydrous minerals. Water in Nominally Anhydrous Minerals, 62, 321-342.
Jacobsen, S.D., Jiang, F., Mao, Z., Duffy, T.S., Smyth, J.R., Holl, C.M., and Frost, D.J. (2008) Effects of hydration on the elastic properties of olivine. Geophysical Research Letters, 35(14).
Jiang, F., Gwanmesia, G.D., Dyuzheva, T.I., and Duffy, T.S. (2009) Elasticity of stishovite and acoustic mode softening under high pressure by Brillouin scattering. Physics of the Earth and Planetary Interiors, 172(3-4), 235-240.
Kawazoe, T., Ohira, I., Ishii, T., Ballaran, T.B., McCammon, C., Suzuki, A., and Ohtani, E. (2017) Single crystal synthesis of δ-(Al, Fe) OOH. American Mineralogist, 102(9), 1953-1956.
Litasov, K., and Ohtani, E. (2003) Stability of various hydrous phases in CMAS pyrolite-H 2 O system up to 25 GPa. Physics and Chemistry of Minerals, 30(3), 147-156.
Mao, Z., Fan, D., Lin, J.-F., Yang, J., Tkachev, S.N., Zhuravlev, K., and Prakapenka, V.B. (2015) Elasticity of single-crystal olivine at high pressures and temperatures. Earth and Planetary Science Letters, 426, 204-215.
Mao, Z., Jacobsen, S., Jiang, F., Smyth, J., Holl, C., and Duffy, T. (2008a) Elasticity of hydrous wadsleyite to 12 GPa: implications for Earth's transition zone. Geophysical Research Letters, 35(21).
Mao, Z., Jacobsen, S.D., Jiang, F., Smyth, J.R., Holl, C.M., Frost, D.J., and Duffy, T.S.

(2008b) Single-crystal elasticity of wadsleyites, beta-Mg2SiO4, containing 0.37-1.66 wt.% H2O. Earth and Planetary Science Letters, 266(1-2), 78-89.

Mao, Z., Lin, J.-F., Jacobsen, S.D., Duffy, T.S., Chang, Y.-Y., Smyth, J.R., Frost, D.J., Hauri, E.H., and Prakapenka, V.B. (2012) Sound velocities of hydrous ringwoodite to 16 GPa and 673 K. Earth and Planetary Science Letters, 331, 112-119.

Marquardt, H., Gleason, A., Marquardt, K., Speziale, S., Miyagi, L., Neusser, G., Wenk, H.R., and Jeanloz, R. (2011) Elastic properties of MgO nanocrystals and grain boundaries at high pressures by Brillouin scattering. Physical Review B, 84(6).

Mashino, I., Murakami, M., and Ohtani, E. (2016) Sound velocities of δ-AlOOH up to core-mantle boundary pressures with implications for the seismic anomalies in the deep mantle. Journal of Geophysical Research: Solid Earth, 121(2), 595-609.

Mookherjee, M., Panero, W.R., Wunder, B., and Jahn, S. (2019) Anomalous elastic behavior of phase egg, AlSiO3(OH), at high pressures. American Mineralogist, 104(1), 130-139.

Ohtani, E. (2020) The role of water in Earth's mantle. National Science Review, 7(1), 224-232.

Ohtani, E., Litasov, K., Suzuki, A., and Kondo, T. (2001) Stability field of new hydrous phase, δ-AlOOH, with implications for water transport into the deep mantle. Geophysical Research Letters, 28(20), 3991-3993.

Ono, S. (1998) Stability limits of hydrous minerals in sediment and mid-ocean ridge basalt compositions: Implications for water transport in subduction zones. Journal of Geophysical Research-Solid Earth, 103(B8), 18253-18267.

Pamato, M.G., Myhill, R., Ballaran, T.B., Frost, D.J., Heidelbach, F., and Miyajima, N. (2015) Lower-mantle water reservoir implied by the extreme stability of a hydrous aluminosilicate. Nature Geoscience, 8(1), 75-79.

Sanchez-Valle, C., Wang, J., and Rohrbach, A. (2019) Effect of calcium on the elasticity of majoritic garnets and the seismic gradients in the mantle transition zone. Physics of the Earth and Planetary Interiors, 293, 106272.

Sano-Furukawa, A., Hattori, T., Komatsu, K., Kagi, H., Nagai, T., Molaison, J.J., dos Santos, A.M., and Tulk, C.A. (2018) Direct observation of symmetrization of hydrogen bond in δ-AlOOH under mantle conditions using neutron diffraction. Scientific reports, 8(1), 1-9.

Sano-Furukawa, A., Kagi, H., Nagai, T., Nakano, S., Fukura, S., Ushijima, D., Iizuka, R., Ohtani, E., and Yagi, T. (2009) Change in compressibility of δ-AlOOH and δ-AlOOD at high pressure: A study of isotope effect and hydrogen-bond symmetrization. American Mineralogist, 94(8-9), 1255-1261.

Sano, A., Ohtani, E., Kondo, T., Hirao, N., Sakai, T., Sata, N., Ohishi, Y., and Kikegawa, T. (2008) Aluminous hydrous mineral δ-AlOOH as a carrier of hydrogen into the core-mantle boundary. Geophysical Research Letters, 35(3).

Sano, A., Ohtani, E., Kubo, T., and Funakoshi, K.-i. (2004) In situ X-ray observation of decomposition of hydrous aluminum silicate AlSiO3OH and aluminum oxide hydroxide d-AlOOH at high pressure and temperature. Journal of Physics and Chemistry of Solids, 65(8-9), 1547-1554.

Schmidt, M.W., Finger, L.W., Angel, R.J., and Dinnebier, R.E. (1998) Synthesis, crystal structure, and phase relations of AlSiO3OH, a high-pressure hydrous phase. American Mineralogist, 83(7-8), 881-888.

Schmidt, M.W., and Poli, S. (1998) Experimentally based water budgets for dehydrating slabs and consequences for arc magma generation. Earth and Planetary Science Letters, 163(1-4), 361-379.

Schulze, K., Pamato, M.G., Kurnosov, A., Ballaran, T.B., Glazyrin, K., Pakhomova, A., and Marquardt, H. (2018) High-pressure single-crystal structural analysis of AlSiO3OH phase egg. American Mineralogist, 103(12), 1975-1980.

Sinogeikin, S., Katsura, T., and Bass, J.D. (1998) Sound velocities and elastic properties of Fe-bearing wadsleyite and ringwoodite. Journal of Geophysical Research: Solid Earth, 103(B9), 20819-20825.

Sinogeikin, S.V., Zhang, J., and Bass, J.D. (2004) Elasticity of single crystal and polycrystalline MgSiO3 perovskite by Brillouin spectroscopy. Geophysical Research Letters, 31(6).

Suzuki, A., Ohtani, E., and Kamada, T. (2000) A new hydrous phase δ-AlOOH synthesized at 21 GPa and 1000 C. Physics and Chemistry of Minerals, 27(10), 689-693.

Tsuchiya, J., and Tsuchiya, T. (2009) Elastic properties of δ-AlOOH under pressure: First principles investigation. Physics of the Earth and planetary interiors, 174(1-4), 122-127.

Vanpeteghem, C.B., Ohtani, E., Kondo, T., Takemura, K., and Kikegawa, T. (2003) Compressibility of phase Egg AlSiO3OH: Equation of state and role of water at high pressure. American Mineralogist, 88(10), 1408-1411.

Wang, J., Bass, J.D., and Kastura, T. (2014) Elastic properties of iron-bearing wadsleyite to 17.7 GPa: Implications for mantle mineral models. Physics of the Earth and Planetary Interiors, 228, 92-96.

Whitfield, C.H., Brody, E.M., and Bassett, W.A. (1976) Elastic moduli of NaCl by Brillouin scattering at high pressure in a diamond anvil cell. Review of Scientific Instruments, 47(8), 942-947.

Wirth, R., Vollmer, C., Brenker, F., Matsyuk, S., and Kaminsky, F. (2007) Inclusions of nanocrystalline hydrous aluminium silicate "Phase Egg" in superdeep diamonds from Juina (Mato Grosso State, Brazil). Earth and Planetary Science Letters, 259(3-4), 384-399.

Wu, Y., Yang, J., Wu, X., Song, M., Yoshino, T., Zhai, S., Qin, S., Huang, H., and Lin, J.F. (2016) Elasticity of single-crystal NAL phase at high pressure: A potential source of the seismic anisotropy in the lower mantle. Journal of Geophysical Research: Solid Earth, 121(8), 5696-5707.

Yuan, H., Zhang, L., Ohtani, E., Meng, Y., Greenberg, E., and Prakapenka, V.B. (2019) Stability of Fe-bearing hydrous phases and element partitioning in the system MgO–Al2O3–Fe2O3–SiO2–H2O in Earth's lowermost mantle. Earth and Planetary Science Letters, 524, 115714.

Zhai, S., and Ito, E. (2008) Phase relations of CaAl4Si2O11 at high-pressure and high-temperature with implications for subducted continental crust into the deep mantle.

Physics of the Earth and Planetary Interiors, 167(3-4), 161-167.
Zhang, J.S., and Bass, J.D. (2016) Single-crystal elasticity of natural Fe-bearing orthoenstatite across a high-pressure phase transition. Geophysical Research Letters, 43(16), 8473-8481.
Zhang, Y., Fu, S., Wang, B., and Lin, J.-F. (2021) Elasticity of a Pseudoproper Ferroelastic Transition from Stishovite to Post-Stishovite at High Pressure. Physical Review Letters, 126(2), 025701.

Tables

Table 1. Elastic properties of phase Egg and δ-AlOOH at ambient conditions.

	Phase Egg		δ-AlOOH	
	This study	Mookherjee et al. (2019)	This study	Tsuchiya et al. (2009)
ρ (g/cm^3)	3.740(2)	3.798	3.536(1)	3.383
C_{11} **(GPa)**	467.2(15)	504.7	375.9(9)	314
C_{22} **(GPa)**	220.8(8)	280.4	295.4(11)	306
C_{33} **(GPa)**	305.2(7)	401.0	433.5(12)	391
C_{44} **(GPa)**	109.8(4)	150.3	129.2(6)	117
C_{55} **(GPa)**	166.0(5)	174.0	133.4(7)	115
C_{66} **(GPa)**	139.6(5)	159.7	166.4(6)	152
C_{12} **(GPa)**	115.9(9)	98.6	49.7(9)	34
C_{13} **(GPa)**	164.3(9)	141.6	91.9(15)	95
C_{23} **(GPa)**	26.3(7)	87.9	52.8(21)	67
C_{15} **(GPa)**	3.2(6)	7.5		
C_{25} **(GPa)**	20.9(9)	13.5		
C_{35} **(GPa)**	21.2(4)	19.8		
C_{46} **(GPa)**	13.7(4)	18.6		
K_{Voigt} **(GPa)**	178.5(8)	204.7	166.0(13)	155.9
G_{Voigt} **(GPa)**	128.9(3)	154.0	146.5(3)	131.1
K_{Reuss} **(GPa)**	138.2(8)	188.2	159.8(13)	151.2
G_{Reuss} **(GPa)**	117.0(3)	148.4	144.0(3)	128.8
K_{VRH} **(GPa)**	158.3(8)	196.4	162.9(13)	153.5
G_{VRH} **(GPa)**	123.0(3)	151.2	145.2(3)	130.0
V_P **(km/s)**	9.28(2)	10.25	10.04(2)	9.83
V_S **(km/s)**	5.73(1)	6.32	6.41(2)	6.20

Figure 1. Representative Brillouin spectra of (a) Phase Egg, (b) δ-AlOOH. The V_S of diamond are marked with D.

Figure 2. The measured velocities of single-crystal phase Egg as a function of the azimuthal angle in crystallographic plane. Dash lines are calculated using the fitting elastic value.

Figure 3. The measured velocities of single-crystal δ-AlOOH as a function of the azimuthal angle in crystallographic plane. Dash lines are calculated using the fitting elastic value.

Figure 1

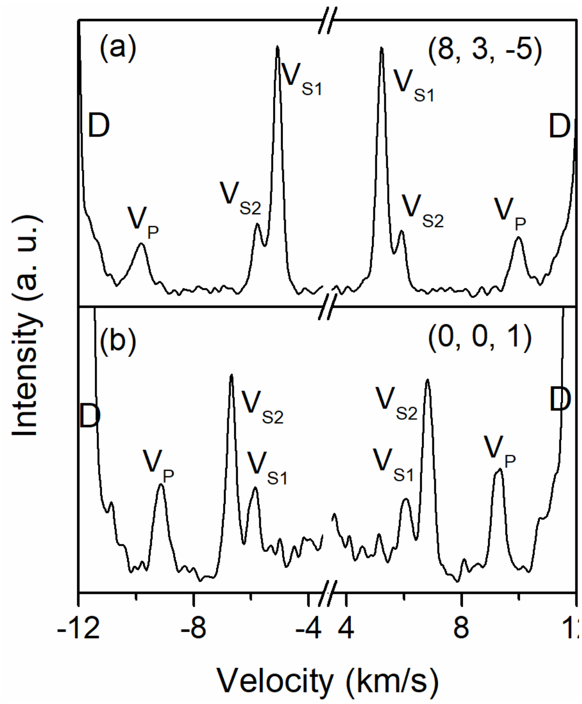
(a)
(8, 3, -5)
D
D
V S1
V S1
V S2
V S2
V P
V P
(b)
(0, 0, 1)
D
D
V S2
V S2
V S1
V S1
V P
V P
Intensity (a. u.)
-12
-8
-4
4
8
Velocity (km/s)

Figure 2

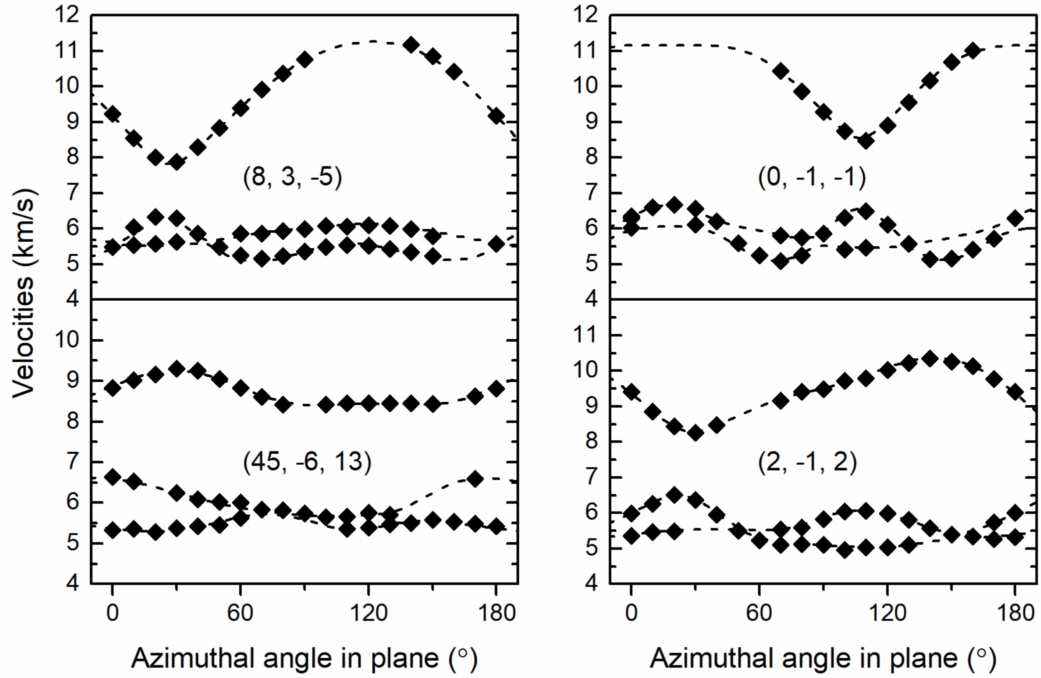

Velocities (km/s)
(8, 3, -5)
(0, -1, -1)
(45, -6, 13)
(2, -1, 2)
Azimuthal angle in plane (°)
Azimuthal angle in plane (°)

Figure 3

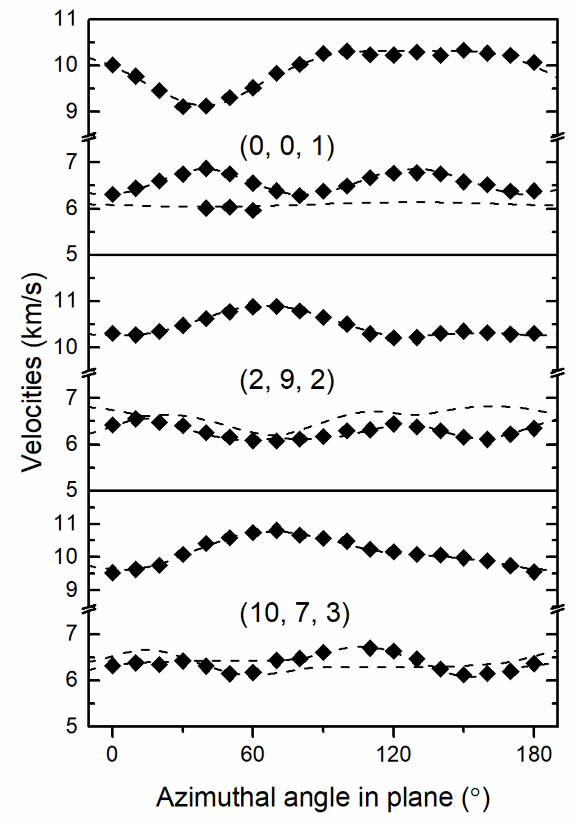

Velocities (km/s)
(0, 0, 1)
(2, 9, 2)
(10, 7, 3)
Azimuthal angle in plane (°)
0
60
120
180
5
6
7
9
10
11

Table S1. Elastic property, seismic velocity and anisotropy of typical mantle minerals at ambient condition.

Mineral	Composition	ρ (g/cm^3)	K_S (GPa)	G (GPa)	V_P (km/s)	V_S (km/s)	AV_P	AV_S	Reference
Olivine	$(Mg_{0.9}Fe_{0.1})_2SiO_4$	3.343	129.6	77.8	8.35	4.82	24.3	18.0	Mao et al. (2015)
Enstatite	$(Mg_{1.74}Fe_{0.16}Al_{0.05}Ca_{0.04}Cr_{0.02})(Si_{1.94}Al_{0.06})O_6$	3.288	112.5	75.9	8.06	4.80	14.0	13.7	Zhang et al. (2016)
Diopside	$Ca_{0.99}Mg_{0.79}Fe_{0.21}Si_{2.01}O_6$	3.345	117.0	70.0	7.92	4.57	25.9	21.2	Fan et al. (2020)
Wadsleyite	$(Mg_{0.915}Fe_{0.075})_2SiO_4$	3.570	170.1	108.0	9.38	5.50	19.0	17.5	Wang et al. (2014)
Hydrous wadsleyite	0.84 wt.% H_2O	3.435	160.4	105.4	9.36	5.54	15.8	15.6	Mao et al. (2008)
Ringwoodite	$(Mg_{0.91}Fe_{0.09})_2SiO_4$	3.701	188.3	119.6	9.69	5.68	4.7	10.3	Sinogeikin et al. (1998)
Hydrous ringwoodite	$(Mg_{1.633}Fe^{2+}_{0.231}Fe^{3+}_{0.026})$ $Si_{1.00}H_{0.179}O_4$	3.649	175.0	106.0	9.31	5.39	4.6	10.4	Mao et al. (2012)
Majorite	$(Ca_{0.39}$ $Mg_{2.66})((Mg,Si)_{0.84}Al_{1.14})Si_3O_{12}$	3.460	159.0	87.1	8.92	5.02	0.3	0.7	Sanchez-Valle et al. (2019)
Pyrope	$Mg_{3.006}Al_{1.995}Si_{3.005}O_{12}$ (900 ppmw H2O)	3.557	168.6	92.3	9.05	5.09	0.9	2.1	Fan et al. (2019)
Bridgmanite	$MgSiO_3$	4.106	253.6	175.0	10.89	6.53	7.6	15.4	Sinogeikin et al. (2004)
Ferropericlase	$Mg_{0.94}Fe_{0.06}O$	3.723	163.3	121.0	9.34	5.70	11.7	23.9	Jackson et al. (2006)
Stishovite	SiO_2	4.301	308.2	228.1	11.93	7.28	25.6	34.2	Jiang et al. (2009)
NAL	$Na_{0.71}Mg_{2.05}Al_{4.62}Si_{1.16}Fe^{2+}_{0.09}Fe^{3+}_{0.17}O_{12}$	3.870	213.1	132.1	10.02	5.84	14.7	15.1	Wu et al. (2016)
Phase Egg	$Al_{0.981}Si_{1.008}O_4H_{1.022}$	3.740	158.3	123.0	9.28	5.73	38.4	22.1	this study
δ-AlOOH	AlOOH	3.536	162.9	145.2	10.04	6.41	19.1	12.7	this study

Figure S1. (a) The structure of phase Egg. (b) The SiO_6 octahedron in phase Egg, the length of Si-O bonds are shown (Schmidt et al., 1998). (c) The structure of δ-AlOOH. The Al, Si and O atoms are shown in gray, blue and red, respectively. The H atoms are small white spheres.

Figure S2. Upper hemisphere pole figures of compressional wave (V_P), shear wave (V_{S1}, V_{S2}) and shear wave splitting (V_S) anisotropy of phase Egg.

Figure S3. Upper hemisphere pole figures of compressional wave (V_P), shear wave (V_{S1}, V_{S2}) and shear wave splitting (V_S) anisotropy of δ-AlOOH.

Figure S1

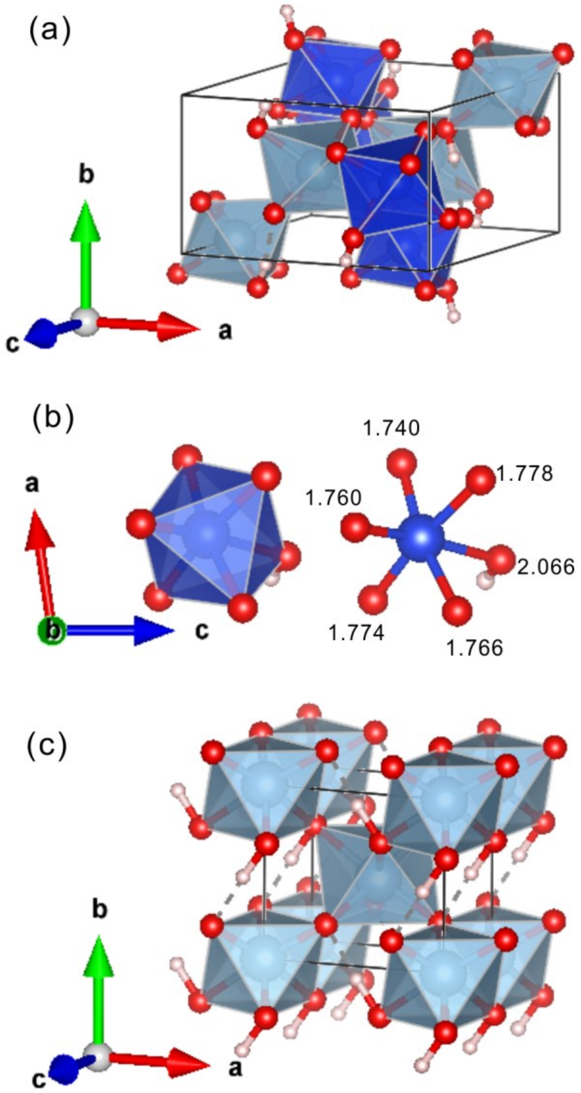

Figure S2

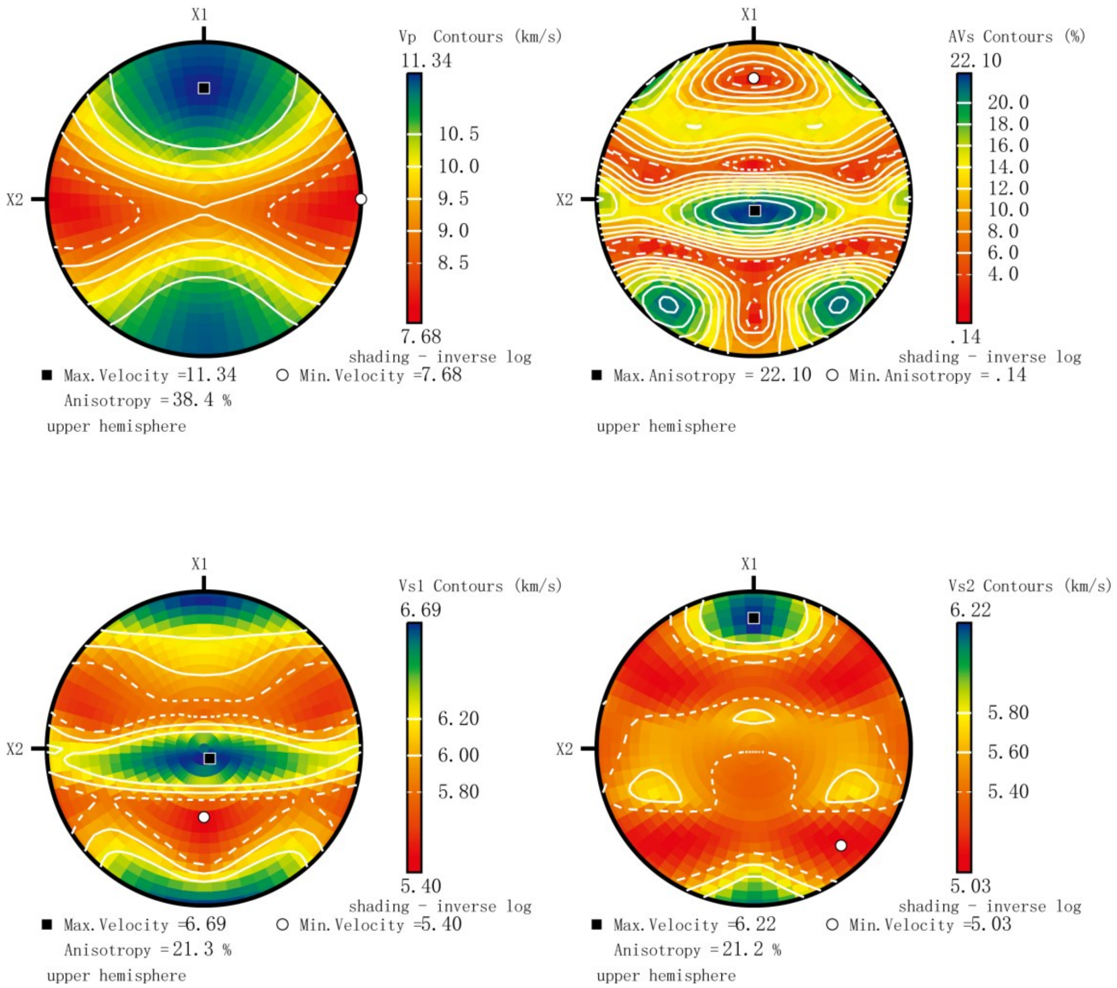
X1
X2
Vp Contours (km/s)
11.34
10.5
10.0
9.5
9.0
8.5
7.68
shading - inverse log
■ Max.Velocity =11.34
○ Min.Velocity =7.68
Anisotropy =38.4 %
upper hemisphere
X1
X2
AVs Contours (%)
22.10
20.0
18.0
16.0
14.0
12.0
10.0
8.0
6.0
4.0
.14
shading - inverse log
■ Max.Anisotropy = 22.10
○ Min.Anisotropy = .14
upper hemisphere
X1
X2
Vs1 Contours (km/s)
6.69
6.20
6.00
5.80
5.40
shading - inverse log
■ Max.Velocity =6.69
○ Min.Velocity =5.40
Anisotropy =21.3 %
upper hemisphere
X1
X2
Vs2 Contours (km/s)
6.22
5.80
5.60
5.40
5.03
shading - inverse log
■ Max.Velocity =6.22
○ Min.Velocity =5.03
Anisotropy =21.2 %
upper hemisphere

Figure S3

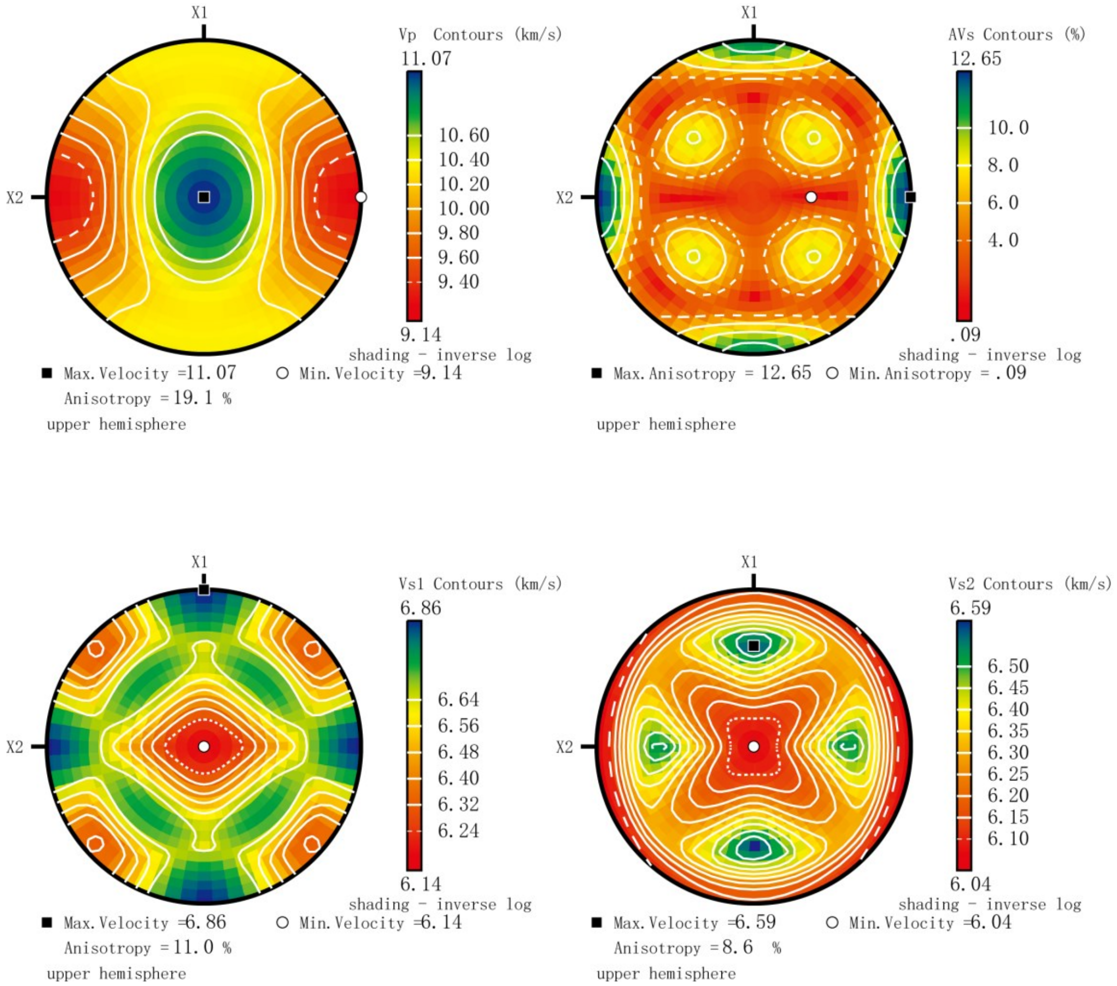
X1
X2
Vp Contours (km/s)
11.07
10.60
10.40
10.20
10.00
9.80
9.60
9.40
9.14
shading - inverse log
■ Max.Velocity =11.07 ○ Min.Velocity =9.14
Anisotropy =19.1 %
upper hemisphere
X1
X2
AVs Contours (%)
12.65
10.0
8.0
6.0
4.0
.09
shading - inverse log
■ Max.Anisotropy = 12.65 ○ Min.Anisotropy = .09
upper hemisphere
X1
X2
Vs1 Contours (km/s)
6.86
6.64
6.56
6.48
6.40
6.32
6.24
6.14
shading - inverse log
■ Max.Velocity =6.86 ○ Min.Velocity =6.14
Anisotropy =11.0 %
upper hemisphere
X1
X2
Vs2 Contours (km/s)
6.59
6.50
6.45
6.40
6.35
6.30
6.25
6.20
6.15
6.10
6.04
shading - inverse log
■ Max.Velocity =6.59 ○ Min.Velocity =6.04
Anisotropy =8.6 %
upper hemisphere